

This is the accepted manuscript made available via CHORUS. The article has been published as:

van der Waals bilayer energetics: Generalized stacking-fault energy of graphene, boron nitride, and graphene/boron nitride bilayers

Songsong Zhou, Jian Han, Shuyang Dai, Jianwei Sun, and David J. Srolovitz

Phys. Rev. B **92**, 155438 — Published 30 October 2015

DOI: [10.1103/PhysRevB.92.155438](https://doi.org/10.1103/PhysRevB.92.155438)

Van der Waals Bilayer Energetics: generalized stacking-fault energy of graphene, boron nitride and graphene/boron nitride bilayers

Songsong Zhou¹, Jian Han¹, Shuyang Dai¹, Jianwei Sun², and David J. Srolovitz^{1,3}

¹*Department of Materials Science and Engineering,*

University of Pennsylvania, Philadelphia, Pennsylvania 19104, USA

²*Department of Physics, Temple University, Philadelphia, Pennsylvania 19122, USA*

³*Department of Mechanical Engineering and Applied Mechanics,
University of Pennsylvania, Philadelphia, Pennsylvania 19104, USA*

(Dated: September 4, 2015)

The structure, thermodynamics and band gaps in graphene/graphene (G/G), boron nitride/boron nitride (BN/BN), and graphene/boron nitride (G/BN) bilayers are determined using several different corrections to first-principles approaches to account for the dispersion interactions. While the density functional dispersion correction (DFT-D2), van der Waals density functional (vdW-DF2), meta-generalized gradient approximation (MGGA-MS2) and adiabatic fluctuation-dissipation theorem methods (ACFDT-RPA) all lead to qualitatively similar predictions, the best accuracy is obtained through the application of the computationally expensive ACFDT-RPA method. We present an accurate ACFDT-RPA-based method to determine bilayer structure, generalized stacking-fault energy (GSFE) and band gaps as a function of the relative translation states of the two layers. The GSFE data clearly identifies all of the stable and metastable bilayer translations as well as the barriers between them. This is key for predicting the sliding, formation and adhesion energies for homo- and hetero-bilayers as well as for the determination of defects in such multilayer van der Waals systems. These, in turn, provide an accurate approach for determining and manipulating the spatial variation of electronic structure.

PACS numbers: PACS appear here

I. INTRODUCTION

Bilayer systems, such as homo-bilayer graphene (G/G), homo-bilayer boron nitride (BN/BN), and hetero-bilayer graphene/boron nitride (G/BN), show promise for applications in electronic nanodevices. Bilayer graphene has been employed in field-effect transistors and optoelectronics for its negligible effective mass^{1,2} and unique quantum Hall effect³⁻⁶. Boron nitride has large band gap and provides an atomically flat surface, which makes it an appealing substrate for nanodevices^{7,8}. Hetero-bilayer G/BN devices possess a favorable band-gap opening, higher carrier mobility, and an improved on/off ratio, compared with conventional silicon-based graphene devices^{8,9}. Building bilayer devices inevitably involves mechanical processes such as rotation and translation of one layer relative to the other. This has substantial influence on the performance and quality of such devices^{10,11}. For example, rotation between the layers in bilayer graphene commonly occurs by design or default. Such rotation gives rise to structural Moiré patterns which directly affect the electronic properties of bilayers^{12,13}. In this report, we focus primarily on the structural and mechanical aspects of bilayers, including the influence on bilayer energy, interlayer spacing, and band gap in the G/G and BN/BN homo-bilayers, and the G/BN hetero-bilayer.

The generalized stacking-fault energy (GSFE) is the difference of energy (per area) between the ground-state structure and the uniformly disregistered structure (dis-

registry refers to the relative displacement of one layer with respect to the other)¹⁴. The GSFE landscape provides information on the preferred directions of disregistry as well as the barriers between the metastable disregistry states. The relaxed bilayer structure is a compromise between the GSFE, that tends to keep the layers registered, and the elastic strain energy required to do so. We note that the GSFE is a local property; it describes the mechanical response at any local position within the bilayer structure. As such, the GSFE plays a key role in determining bilayer structure under any kind of deformation (homogeneous or inhomogeneous, flat or curved). While this is obviously important for hetero-bilayers, where the layers have different lattice constant (leading to the formation of misfit dislocations), it also applies to homo-bilayers. As in the case of twist grain boundaries in bulk materials^{15,16}, the GSFE plays a fundamental role in determining the structure, energetics and properties of homo-bilayers where one layer is rotated with respect to the other¹⁷. The mechanically-relaxed bilayer structure must be determined before local electronic and optical properties can be reliably determined. Therefore, accurate determination of the GSFE is necessary in order to predict the structure and the mechanical, electrical and/or optical properties of flat, curved, misfitting, and twisted bilayers.

The calculation of GSFEs has been reported for a few bilayer systems. While these earlier studies provide important information and insight, two major issues remain that prevent the general application of these GSFEs to

accurately determine the structure and properties of bilayers (discussed above).

First, the effect of interlayer spacing on GSFEs has not been fully accounted for. In both hetero-bilayer and twisted homo-bilayer systems, the interlayer spacing varies through the layer – especially near the dislocation cores. In other applications, the interlayer spacing varies with application of stress/strain in the bilayer plane of the bilayer (Poisson effect) or normal to this plane (e.g., at contacts or during friction experiments¹⁸). In most of the existing studies GSFEs were obtained at fixed interlayer spacing^{19,20}. However, in a few recent GSFE calculations, the interlayer spacing was fully relaxed (normal to the bilayer plane) for each disregistry state^{21,22}. While this is an important step, a complete description of GSFE should include interlayer spacing as a variable (rather than a parameter predetermined). Recent results in bulk materials show that the GSFE is sensitive to this variable^{23,24}. Although ideally the GSFE obtained for fully relaxed interlayer spacing corresponds to the case of free-standing bilayers, the GSFE at different strains (normal to the bilayer plane) is critical for describing bilayer under mechanical load and local structures within bilayers (such as near dislocation cores).

Second, conventional DFT does not account for the dispersion interactions which dominate interlayer interactions in van der Waals solids^{25,26}. This can be easily understood from the fact that dispersion interactions arise from instantaneous polarization multipoles, which involve dynamic correlations not captured by conventional density functionals²⁷. Thus, reliable GSFE landscapes based on conventional DFT cannot be directly applied to van der Waals bilayer systems. Many approaches have been suggested to correct this shortcoming. The Grimme’s density functional dispersion correction (DFT-D2) adds a semi-empirical term to the conventional Kohn-Sham (KS) energy to account for dispersion interactions²⁸, while the non-local van der Waals density functionals (vdW-DF2) captures the long-range van der Waals interactions without relying on empirical input^{29,30}. Recently, the meta-generalized gradient approximation (MGGA-MS2) was shown to capture much of the intermediate-range van der Waals interactions we are interested in here^{31–33}. The adiabatic-connection fluctuation-dissipation theorem within the random phase approximation (ACFDT-RPA) has been shown to provide a reliable description of dispersion interactions^{34–36}. Although DFT-D2 (or similar approaches) is computationally much less costly than ACFDT-RPA, it has yet to be demonstrated whether this approach can be used to give quantitatively reliable GSFEs. While the ACFDT-RPA should be considered a benchmark against which such calculations can be compared, the considerable computational resources required for such calculation makes it extremely difficult to obtain the GSFE using ACFDT-RPA.

In this paper, we describe the development of an approach to obtain bilayer GSFEs that address the short-

comings of earlier studies; i.e., to obtain GSFE that are both accurate and general. We present calculations of the GSFE landscapes and the energy versus interlayer spacing for G/G, BN/BN, and G/BN bilayer systems based on four different correction methods, i.e., DFT-D2, vdW-DF2, MGGA-MS2, and ACFDT-RPA. While ACFDT-RPA has been shown to be more accurate than the other approaches, we perform such a comparison to determine if these less computationally costly approaches yield the qualitatively correct GSFE and to determine whether the quantitative differences are sufficient to justify the additional cost. In short, we find that, while one of the methods leads to qualitatively incorrect results (e.g., incorrect ordering of the energies of several high-symmetry disregistry states), the other methods lead to significant quantitative errors (with respect to the more accurate ACFDT-RPA results and each other). Next, we proceed to the determination of accurate GSFE landscapes and interlayer spacing based on ACFDT-RPA calculations. We propose an analytical symmetry-respecting description of these landscapes that can be accurately parameterized with a small number of ACFDT-RPA calculations. This leads to a description of the bilayer GSFE and its dependence on interlayer spacing that is suitable for use in multiscale methodologies for determining the structure and properties of strained and dislocated bilayer systems. The effectiveness of this function is validated by detailed comparison of these analytical GSFE landscapes and first-principles results. Finally, we show an example of how to apply this approach to determine how shifts (disregistry) between the layers affect properties; in this case we focus on the band gap.

II. COMPUTATIONAL DETAILS

We examined the efficacy of several competing DFT methods for determination of the GSFE and the relaxed interlayer spacing as a function of disregistry. DFT-D2 simply adds a semi-empirical term to the KS energy to account for the missing long-range interactions. DFT-D2 provides better results than conventional density functionals with little added computational cost. Unlike conventional functionals in the local density approximation (LDA) or generalized gradient approximation (GGA), the total exchange-correlation energy in vdW-DF2 is separated into semi-local and non-local terms. The semi-local term limits the gradient corrections to the exchange term and a non-local term captures the correlation that involves the electrodynamic coupling^{29,37,38}. The semi-local MGGA functional adds the kinetic energy density of the occupied orbitals as input, whereas conventional GGA uses only the density and the corresponding gradient as input³². Because the kinetic energy density enables the MGGA functional to capture the intermediate-range van der Waals interaction, and the MGGA functional should be suitable for studying weakly bonded layered materials^{39,40}. The ACFDT-RPA is derived from

TABLE I. The parameters used in the bilayer calculations for each correction method

Method	G/G		BN/BN		G/BN	
	E_{cut} (eV)	k -mesh	E_{cut} (eV)	k -mesh	E_{cut} (eV)	k -mesh
DFT-D2	500	$36 \times 24 \times 1$	700	$24 \times 14 \times 2$	720	$24 \times 14 \times 2$
vdW-DF2	680	$20 \times 12 \times 3$	800	$20 \times 12 \times 2$	780	$20 \times 12 \times 2$
MGGA-MS2	800	$20 \times 12 \times 3$	640	$24 \times 14 \times 2$	420	$20 \times 12 \times 2$
ACFDT-RPA exchange	540	$16 \times 16 \times 2$	540	$16 \times 16 \times 2$	540	$16 \times 16 \times 2$
ACFDT-RPA correlation	400	$12 \times 12 \times 1$	440	$12 \times 12 \times 1$	420	$12 \times 12 \times 1$

the adiabatic-connection fluctuation-dissipation theorem within a direct random phase approximation³⁴. Such calculations involve two distinct parts. The correlation energy is described by

$$E_c = \frac{1}{2\pi} \int_0^\infty dw \text{Tr} \{ \ln [1 - \chi^0(iw)v] + \chi^0(iw)v \}, \quad (1)$$

where Tr indicates the trace, χ^0 is the independent particle response function and v is the Coulomb kernel. The exchange energy E_x is calculated within the Hartree-Fock approach. Both parts are evaluated using the Perdew-Burke-Ernzerhof (PBE) orbital to find the total ground-state energy $E = E_x + E_c$. Previous research^{35,36,41} suggests that ACFDT-RPA should provide the most accurate description of the dispersion interactions. However, this method requires substantially more computational resources than the other methods, described above.

All of the calculations were performed using the KS orbitals from an initial calculation with the PBE functional⁴², followed by application of the correction methods. The calculations were performed using the Vienna *ab initio* simulation package (VASP)^{43–46} with the projector-augmented wave method^{47,48}. The detailed calculation parameters for all the correction methods are summarized in Table I. The cutoff energy (E_{cut}) and k -meshes were optimized to ensure that the energy converges to within 1 meV. We explicitly assume that each layer in the bilayer is flat and that the two layers are parallel to one another in all of the calculations.

III. COMPARISON OF COMPUTATIONAL METHODS

We first calculated the in-plane lattice parameter a_0 and the equilibrium interlayer spacing d_0 using all four correction methods described above. (Note, for the G/BN case, we strain the two layers to match lattice parameters and minimize the energy with respect to the matched lattice parameter.) For the cases where ACFDT-RPA was used, a_0 was optimized using the standard PBE functional while d_0 was optimized using the ACFDT-RPA method. These calculations were first performed based upon the experimentally observed layer registry^{51,54}; referring to Fig. 1, these are AB for G/G, AA' for BN/BN, and AB for G/BN. The values of a_0 and

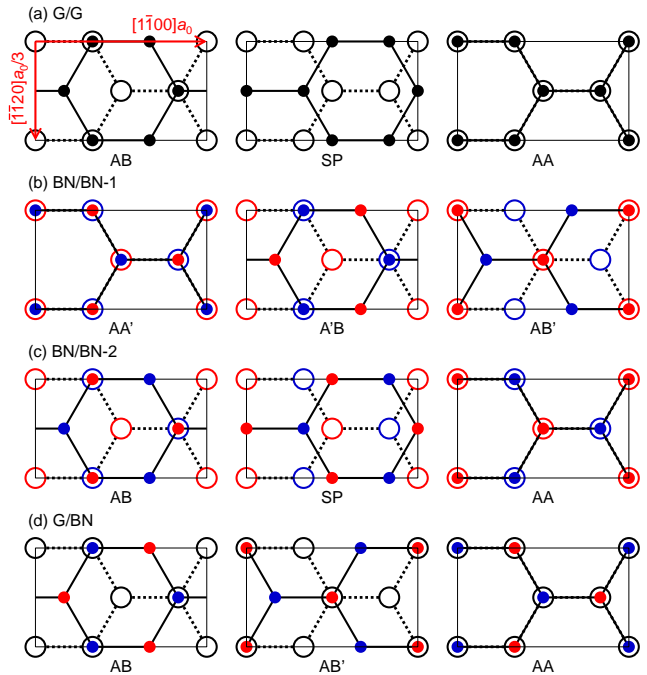


FIG. 1. Schematic representation of several high-symmetry configurations of (a) G/G, (b) BN/BN-1, (c) BN/BN-2, and (d) G/BN. The three figures for each bilayer correspond to different registry states (registries resulting from the relative displacements of the layers along the $[1\bar{1}00]$ direction). The black, blue, and red circles represent C, N, and B atoms, respectively. The larger, open circles connected by dashed lines represent atoms in the lower layer and the smaller solid circles connected by solid lines represent atoms in the upper layer.

d_0 obtained are summarized in Table II. All the methods reproduce the experimentally measured in-plane lattice parameters (a_0) to within better than 1%. However, the equilibrium interlayer spacings (d_0) show a variation of approximately 10% between the methods for all three bilayer systems. In each case, d_0 is underestimated by DFT-D2 and overestimated by vdW-DF2 and MGGA-MS2, as compared with the experimental values. In contrast, the values of d_0 obtained using ACFDT-RPA are in excellent agreement (to within 0.1 Å) with the experimental results for all three bilayer systems^{49,51,53}.

We also calculated the $\mathbf{n} \otimes \mathbf{n}$ component of the elastic constant tensor $C_{nn,0}$ (\mathbf{n} is the bilayer normal; con-

TABLE II. The in-plane lattice parameter a_0 (Å), the equilibrium interlayer spacing d_0 (Å), the $\mathbf{n} \otimes \mathbf{n}$ component of the equilibrium elastic constant tensor $C_{nn,0}$ (GPa), and the cohesive energy per area γ_{coh} (mJ/m²) for bilayer G/G, BN/BN, and G/BN as determined using the four correction methods and from experimental data. Each calculation was performed for the experimentally observed registry state; i.e., AB for G/G, AA' for BN/BN, and AB for G/BN (see Fig. 1).

Method	G/G				BN/BN				G/BN			
	a_0	d_0	$C_{nn,0}$	γ_{coh}	a_0	d_0	$C_{nn,0}$	γ_{coh}	a_0	d_0	$C_{nn,0}$	γ_{coh}
DFT-D2	2.46	3.25	38	308.9	2.51	3.12	55	402.5	2.49	3.14	44	373.8
vdW-DF2	2.47	3.55	30	297.3	2.52	3.51	24	291.6	2.50	3.51	36	298.9
MGGA-MS2	2.45	3.59	12	47.86	2.50	3.51	17	58.48	2.48	3.49	12	63.56
ACFDT-RPA	2.46 ^a	3.39	30	558.5	2.50 ^a	3.34	46	222.7	2.49 ^a	3.32	33	345.4
Experimental data	2.46 ^{49b}	3.34 ^{49b}	36.5 ± 1.0 ^{50b}		2.50 ^{51b}	3.33 ^{51b}	32 ± 3 ^{52b}			3.32 ^{53c}		

^a These data were obtained using the standard PBE functional.

^b These experimental data were obtained for bulk materials (graphite or hexagonal boron nitride) rather than bilayer structures.

^c These experimental data were obtained for heterostructures.

ventionally this is C_{33}) and the cohesive energy per area γ_{coh} in the equilibrium structure (i.e., the first images on the left in Fig. 1). These quantities are defined as $C_{nn,0} = (d_0/A) [d^2 E_{2L}(\delta)/d\delta^2]_{\delta=d_0}$ and $\gamma_{\text{coh}} = [E_{2L}(\infty) - E_{2L}(d_0)]/A$, where $E_{2L}(\delta)$ is the total energy of the bilayer as a function of interlayer spacing δ , and A is the area of each layer in the bilayer. The cohesive energy here refers to the binding energy of the two layers (rather than the energy of binding atoms); this can also be thought of as the cleavage or adhesion energy. The values of $C_{nn,0}$ and γ_{coh} are listed in Table II.

Next, we investigated the GSFE and the relaxed interlayer spacing versus disregistry along the high-symmetry $[1\bar{1}00]$ (armchair) direction as shown in Fig. 2 and Fig. 3, respectively. The corresponding high-symmetry configurations are shown in Fig. 1. For each disregistry, the interlayer spacing was allowed to relax (i.e., we minimized the energy with respect to interlayer spacing at fixed disregistry). For G/G and G/BN, all of the high-symmetry configurations can be transformed into one another by the translation of one layer with respect to the other. However, for BN/BN, some high-symmetry configurations (e.g., AB and AA') cannot be related by translation; in addition to the stable configuration AA' (associated with the minimum in Fig. 2(b)), a non-equivalent stable (metastable) configuration AB exists (associated with the minimum in Fig. 2(c)) corresponding to a 60° rotation of one layer of AA' with respect to the other about an axis going through a pair of atoms (normal to the layer). The set of disregistry states generated from AA' is labeled BN/BN-1 (see Fig. 1(b)); the set of disregistry states generated by AB is labeled BN/BN-2 (Fig. 1(c)).

For G/G and G/BN, all four correction methods indicate that the stable structure is AB. Note that the apparent local minimum in the G/BN GSFE curve along $[1\bar{1}00]$ (Fig. 2(d)) between the AB' and AA states is a saddle point. For BN/BN, the DFT-D2 correction predicts that the stable structure corresponds to the AB state (in BN/BN-2) rather than the AA' state (in BN/BN-1); this contradicts the results from the calculations using all of the other methods. The experimental observation

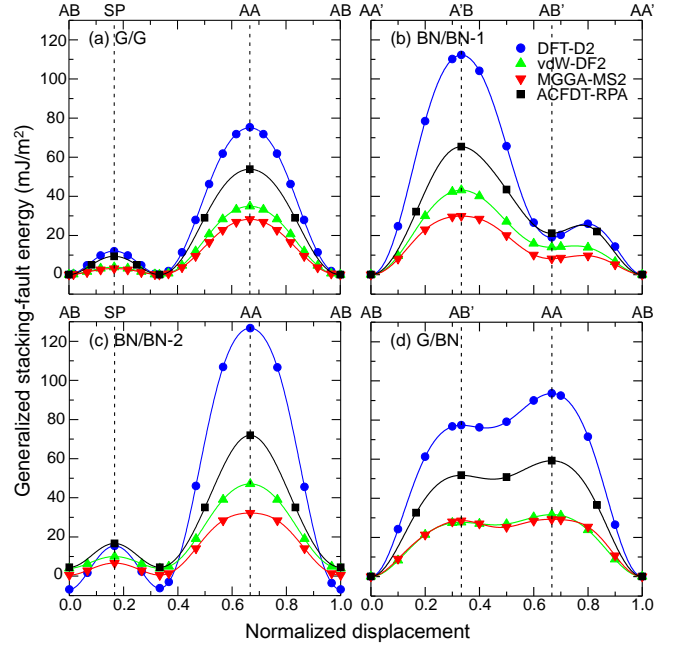


FIG. 2. The GSFE versus disregistry along the $[1\bar{1}00]$ direction for (a) G/G, (b) BN/BN-1, (c) BN/BN-2, and (d) G/BN. For BN/BN-1 and BN/BN-2, the reference configuration was set to be AA' (BN/BN-1).

suggests that AA' stacking is favored in bulk hexagonal boron nitride⁵¹. Recent calculations based on local second-order Møller-Plesset perturbation theory also shows that AA' is the most stable state²⁰. We therefore conclude that the DFT-D2 correction does not yield the correct equilibrium stacking in BN/BN. The other three methods show the same order of stacking energies for BN/BN: AA' and AB are the most and second most stable states, respectively. The energy difference between these two states is very small (1.1–2.6 mJ/m²), which explains why both the AB and AA' polytypes have been observed in experiments⁵¹. In addition, our calculations also show that the AB' state is metastable, with an energy 8.4–20.2 mJ/m² higher than that of the AA' state.

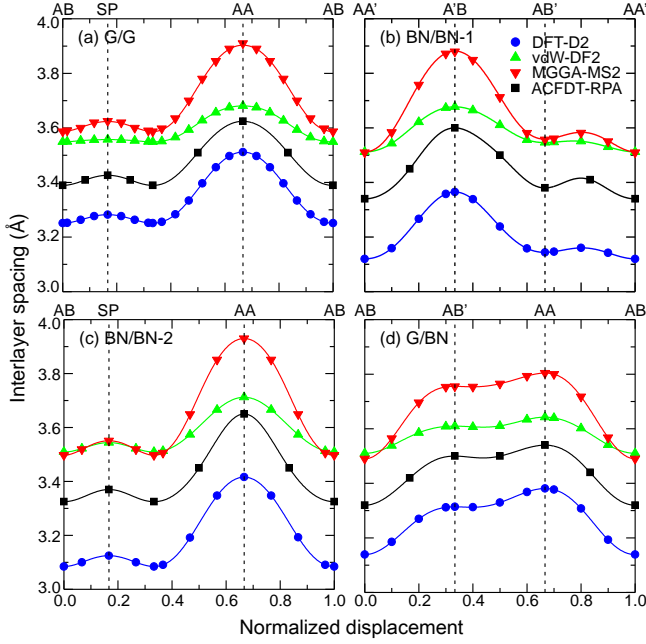


FIG. 3. The relaxed interlayer spacing versus disregistry along the $[1\bar{1}00]$ direction for (a) G/G, (b) BN/BN-1, (c) BN/BN-2, and (d) G/BN.

Figure 3 shows the relaxed interlayer spacing as a function of disregistry along the $[1\bar{1}00]$ direction for all four correction methods. The main features of the relaxed interlayer spacing curves mimic those of the corresponding GSFE curves, i.e., the positions of minima, maxima, and saddle points in the relaxed interlayer spacing curves are also the positions of minima, maxima, and saddle points in the GSFE curves. The observation that significant differences in the values of the relaxed interlayer spacing with different correction methods suggests, not surprisingly, that dispersion interactions are particularly important in determining the relaxed interlayer spacing.

We now draw conclusions from the results in this section. First, since the ACFDT-RPA has been widely shown to reproduce the experimental bulk properties measured for many materials³⁵, including layered systems⁵⁵, we use it as the benchmark for our bilayer studies. We find that, while all of the other methods yield similar qualitative results (see Fig. 2 and Fig. 3), all have serious deficiencies. DFT-D2 predicts a BN/BN stacking order that is inconsistent with experimental observations⁵¹. MGGA-MS2 yields unphysically small bilayer cohesive energies⁵⁶. Using the ACFDT-RPA as the reference, the error in the GSFE profile barrier (i.e., the energy difference between the saddle point and the ground state) is 7%–70% for DFT-D2, 39%–58% for vdW-DF2, and 44%–65% for MGGA-MS2 (the error ranges repre-

sent the different bilayer systems). Therefore, while several of the more computationally efficient alternatives to the ACFDT-RPA yield qualitatively reasonable behavior, they cannot be depended upon to yield quantitatively reliable GSFE and relaxed interlayer spacing for van der Waals bilayer systems. Based on these conclusions, we focus on determining accurate GSFE and relaxed interlayer spacing landscapes based on the ACFDT-RPA. This requires developing an approach that reduces the extremely high computational cost inherent to the ACFDT-RPA approach while retaining the requisite accuracy. This is achieved through the use of the bilayer symmetry and a flexible fitting procedure.

IV. THE GSFE AND RELAXED INTERLAYER SPACING LANDSCAPES

Since ACFDT-RPA is the most accurate method for determining the GSFE and the relaxed interlayer spacing curves along the $[1\bar{1}00]$ direction and its result cannot be quantitatively reproduced by other less costly methods for such calculations, we view it as the only reliable choice for the determination of the full GSFE and relaxed interlayer spacing landscapes. However, performing ACFDT-RPA calculations of these landscapes is too computationally costly to apply over a fine three-dimensional grid of translations. Therefore, we adopted the following strategy. First, we determine the landscapes using the simplest (and least computationally costly) correction method, DFT-D2, the results of which are inaccurate but show the same qualitative trends as the other (more costly) methods. Second, we construct an analytical function to describe these landscapes that respects the structural symmetry. Third, we demonstrate that this function can describe the full landscape with sufficient accuracy with fitting to only a small set of data. Fourth, we obtain the same small set of data using the ACFDT-RPA method. Finally, we generate the GSFE and the relaxed interlayer spacing landscapes by fitting the function to the ACFDT-RPA data for G/G, BN/BN, and G/BN.

The upper panels of Fig. 4 and Fig. 5 show the GSFE and relaxed interlayer spacing landscapes for G/G, BN/BN-1, and G/BN obtained using the DFT-D2 (see Supplemental Material for additional results). These landscapes exhibit the same general features (plane-groups: $p6mm$ for G/G and BN/BN-2, and $p3m1$ for BN/BN-1 and G/BN) except for scale. The GSFE γ and relaxed interlayer spacing d landscapes can be fitted to a symmetry-respecting function $F(\phi, \psi)$, where ϕ and ψ are the disregistries along $[\bar{1}\bar{1}20]$ (zigzag) and $[1\bar{1}00]$ (armchair), respectively:

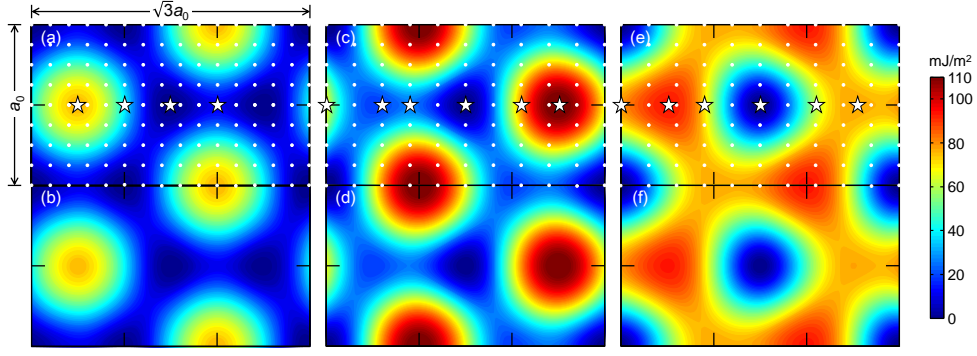


FIG. 4. The GSFE landscapes determined using the DFT-D2 method for (a) G/G, (c) BN/BN-1, and (e) G/BN. All the energies are obtained by relaxing the interlayer spacing. These images are contour plots constructed using the calculation data at the location of the white dots and stars. The best fits of the function form of Eq. (2) to the six/four data points at the positions labeled by the white stars in (a), (c), and (e) are shown in (b), (d), and (f), respectively.

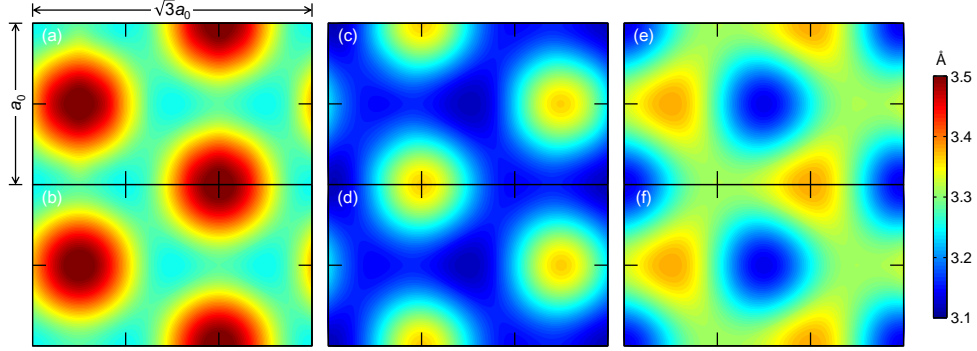


FIG. 5. The relaxed interlayer spacing landscapes determined using the DFT-D2 method for (a) G/G, (c) BN/BN-1, and (e) G/BN corresponding to the GSFE landscapes in Fig. 4. The best fits of the functional form of Eq. (2) to the six/four data points at the positions labeled by the white stars in Figs. 4(a), (c), and (e) are shown in (b), (d), and (f), respectively..

$$\begin{aligned}
 F(\phi, \psi) = & \\
 & c_0 + c_1 \left[\cos \frac{2\pi}{a_0} \left(\phi + \frac{\psi}{\sqrt{3}} \right) + \cos \frac{2\pi}{a_0} \left(\phi - \frac{\psi}{\sqrt{3}} \right) + \cos \frac{4\pi\psi}{\sqrt{3}a_0} \right] + c_2 \left[\cos \frac{2\pi}{a_0} \left(\phi + \sqrt{3}\psi \right) + \cos \frac{2\pi}{a_0} \left(\phi - \sqrt{3}\psi \right) + \cos \frac{4\pi\phi}{a_0} \right] \\
 & + c_3 \left[\cos \frac{2\pi}{a_0} \left(2\phi + \frac{2\psi}{\sqrt{3}} \right) + \cos \frac{2\pi}{a_0} \left(2\phi - \frac{2\psi}{\sqrt{3}} \right) + \cos \frac{8\pi\psi}{\sqrt{3}a_0} \right] + c_4 \left[\sin \frac{2\pi}{a_0} \left(\phi - \frac{\psi}{\sqrt{3}} \right) - \sin \frac{2\pi}{a_0} \left(\phi + \frac{\psi}{\sqrt{3}} \right) + \sin \frac{4\pi\psi}{\sqrt{3}a_0} \right] \\
 & + c_5 \left[\sin \frac{2\pi}{a_0} \left(2\phi - \frac{2\psi}{\sqrt{3}} \right) - \sin \frac{2\pi}{a_0} \left(2\phi + \frac{2\psi}{\sqrt{3}} \right) + \sin \frac{8\pi\psi}{\sqrt{3}a_0} \right], \quad (2)
 \end{aligned}$$

where c_0 – c_5 are constants to be determined by fitting for each bilayer material system. The constant $c_0 = -3(c_1 + c_2 + c_3) + F_0$, where F_0 is the excess energy per area (in reference to the ground state) at $(\phi, \psi) = \mathbf{0}$ when F refers to the GSFE γ , and F_0 is the relaxed interlayer spacing d . This function is the same as that proposed by Xiang *et al.*⁵⁷. While it has the flexibility to describe a landscape with either $p3m1$ or $p6mm$ symmetry, in cases where the symmetry is $p6mm$ (i.e., G/G and BN/BN-2) the number of independent parameters can be reduced from five to three; i.e., $c_4 = \sqrt{3}c_1$ and $c_5 = -\sqrt{3}c_3$.

For the systems with landscapes of $p3m1$ symmetry (BN/BN-1 and G/BN), there are only five independent parameters in the function, so five independent data points should suffice to fit this function for each landscape. For the systems for which the landscapes possess $p6mm$ symmetry, i.e., G/G and BN/BN-2, only three independent data points are needed. In order to validate this approach, we fitted the parameters to six or four non-equivalent data points obtained by DFT-D2 for each landscape (of either GSFE or relaxed interlayer spacing); an extra point was added to improve the fitting quality. The positions of these points were chosen as indicated by

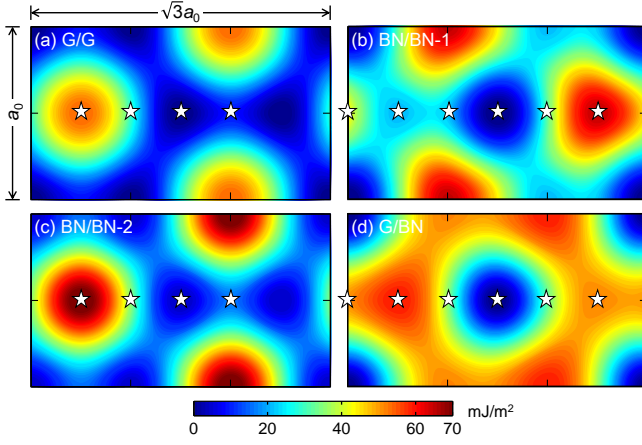


FIG. 6. The GSFE landscapes derived from fitting six or four data points (indicated by white stars) obtained from ACFDT-RPA for (a) G/G, (b) BN/BN-1, (c) BN/BN-2, and (d) G/BN to the function form of Eq. (2).

the white stars in Fig. 4. The fitted GSFE and relaxed interlayer spacing landscapes are shown in the lower panels of Fig. 4 and Fig. 5, respectively (the fitting parameters are reported in the Supplemental Material). Comparison of these fits with the results of direct calculations (upper panels of Fig. 4 and Fig. 5) shows that excellent agreement is obtained over the entire disregistry landscape. This demonstrates the validity and accuracy of the proposed function and fitting procedure.

Given the excellent fits that Eq. (2) provides for the GSFE and relaxed interlayer spacing landscapes based on six or four DFT-D2 data points, we employed the same approach to generate the GSFE and relaxed interlayer spacing landscapes based on the same limited set of data points obtained using the ACFDT-RPA approach. The resultant GSFE and relaxed interlayer spacing landscapes are shown in Fig. 6 and Fig. 7, respectively. The parameters in Eq. (2) obtained using the ACFDT-RPA method are reported in Table III.

There are two minima in the GSFE landscapes of G/G and BN/BN-2 within one period of disregistry; they have exactly the same energy (i.e., the ground-state energy) and the corresponding structures are equivalent. The structure created by displacing the upper layer of the AB configuration with respect to the lower layer (see Fig. 1(a) and (c)) in the $\langle 1\bar{1}00 \rangle$ direction by $a_0/\sqrt{3}$ is equivalent to that created by inverting the stacking order of the AB configuration (i.e., the BA configuration). For BN/BN-1, there is one global minimum and one local minimum corresponding to the stable AA' and metastable AB' states, respectively (see Fig. 1(b)). The local minimum corresponds to an intrinsic stacking fault. The G/BN GSFE landscape exhibits only one minimum; i.e., AB is the only stable state in G/BN and there are no metastable states.

The vector that connects the nearest neighboring global and/or local minima in the GSFE landscape can be interpreted as the Burgers vector of an interlayer dis-

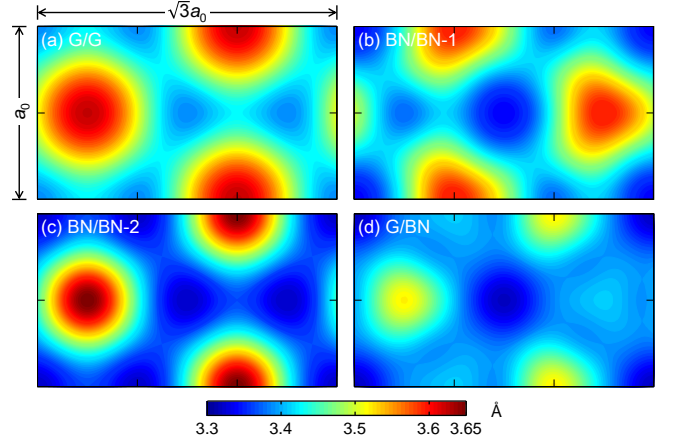


FIG. 7. The relaxed interlayer spacing landscapes derived from fitting six or four data points obtained from ACFDT-RPA for (a) G/G, (b) BN/BN-1, (c) BN/BN-2, and (d) G/BN to the function form of Eq. (2).

TABLE III. The parameters in the fits of Eq. (2) to the ACFDT-RPA data. The units for c_0 – c_5 are mJ/m^2 and \AA in the fits to the data of GSFE and relaxed interlayer spacing, respectively.

Parameter	G/G	BN/BN-1	BN/BN-2	G/BN
GSFE, γ				
c_0	21.336	31.584	28.454	39.222
c_1	-6.127	-9.935	-7.160	-11.96
c_2	-1.128	-0.918	-0.496	-0.748
c_3	0.143	0.325	-0.339	-0.366
c_4	$\sqrt{3}c_1$	-7.848	$\sqrt{3}c_1$	1.640
c_5	$-\sqrt{3}c_3$	0.670	$-\sqrt{3}c_3$	0.201
Relaxed interlayer spacing, d				
c_0	3.47889	3.44998	3.42584	3.45362
c_1	-0.02648	-0.03667	-0.03375	-0.04510
c_2	-0.00352	-0.00333	0.00250	0.00000
c_3	0.00037	0.00334	-0.00236	0.00056
c_4	$\sqrt{3}c_1$	-0.03752	$\sqrt{3}c_1$	0.00866
c_5	$-\sqrt{3}c_3$	0.00481	$-\sqrt{3}c_3$	0.00096

location in the bilayer system (this Burgers vector lies in the bilayer plane). For G/G, BN/BN-1, and BN/BN-2, these are partial dislocations with Burgers vector $\frac{a_0}{3}\langle 1\bar{1}00 \rangle$, implying that dislocation dissociations of the type $\frac{a_0}{3}[\bar{1}120] \rightarrow \frac{a_0}{3}[0\bar{1}10] + \frac{a_0}{3}[\bar{1}010]$ can occur and generate a stacking fault region between the two partials. For G/G and BN/BN-2, the stacking fault structure (corresponding to the BA state) is equivalent to the unfaulted structure (corresponding to the AB state) as shown in Fig. 1. (Note that, since the AB and BA states have the same energy, there is no stacking-fault energy, yet the dislocation corresponding to $\frac{a_0}{3}\langle 1\bar{1}00 \rangle$ should be viewed as a partial dislocation in the sense that this translation is not a full translation vector of the lattice.) In the G/BN case, there is only a single minimum within one disregistry period. The vector connecting the near-

est neighboring minima is $\frac{aa}{3}\langle\bar{1}\bar{1}20\rangle$, corresponding to a full dislocation in this bilayer system (i.e., no dissociation is possible).

The layers in a bilayer can slide relative to one another; for different bilayer systems, the preferred sliding directions are different. Such information is also contained in the GSFE landscape. The preferred sliding directions for G/G and BN/BN-2 are $\langle\bar{1}\bar{1}00\rangle$. The associated energy barriers are symmetric for forward and backward sliding; the barriers are 7.9 mJ/m² and 15.7 mJ/m² for G/G and BN/BN-2, respectively. For BN/BN-1, the preferred sliding direction is also $\langle\bar{1}\bar{1}00\rangle$, but because of the existence of the stacking fault (corresponding to the metastable AB' state) the barriers are asymmetric; the forward-sliding (AA' \rightarrow AB') and backward-sliding (AB' \rightarrow AA') barriers are 25.2 mJ/m² and 4.1 mJ/m², respectively. Finally, for G/BN, sliding occurs in the $\langle\bar{1}\bar{1}20\rangle$ direction with a barrier of 51.1 mJ/m². In practice, sliding is likely to occur via the motion of dislocations rather than rigid sliding of one entire layer. The resistance to sliding should be the Peierls barrier for dislocation motion which, in such systems, is expected to be very low because the dislocation core widths in van der Waals bilayer systems are very large⁵⁸. The rigid sliding case can be thought of as providing the theoretical upper bound on the true sliding resistance.

V. THREE-DIMENSIONAL GSFE

The conventional definition of GSFE is the stacking-fault energy as a function of disregistry at the relaxed interlayer spacing for each disregistry state. However, the out-of-plane separation is also an interesting variable; it is important for evaluating how individual layers are assembled or decreed, for evaluating the ease of intercalating atoms/molecules between the layers of a bilayer, or for understanding the elastic distortion of the bilayer upon introduction of defects. The stacking-fault energy is sensitive to strain^{23,24}. To enable the application of first-principles input for bilayer deformation more general than pure sliding, we extended the two-dimensional GSFE to three dimensions, i.e., $\gamma(\phi, \psi) \rightarrow \Gamma(\phi, \psi, \delta)$, where δ is the variable interlayer spacing.

Γ is the excess energy per area relative to the equilibrium configuration (i.e., AB for G/G, AA' for BN/BN, or AB for G/BN). We propose a simple form for the dependence of Γ on δ

$$\Gamma(\phi, \psi, \delta) = A \exp(-\alpha\delta) - B \left(\frac{d}{\delta}\right)^4 + \gamma_{\text{coh}}, \quad (3)$$

where A , B , and α are functions of ϕ and ψ and $d(\phi, \psi)$ is the relaxed interlayer spacing. The first term in Eq. (3) is of the Morse-potential type, an empirical description of the short-range repulsion. The second term guarantees that the energy converges to the functional form expected for the long-range part of the van der Waals interaction.

The power in the van der Waals term (δ^{-4}), results from the double integral of the classical r^{-6} interatomic form to account for the interaction between two layers. We note that the power law for graphite has been reported⁴¹ to be $\delta^{-4.2}$ for $3 \text{ \AA} \leq \delta \leq 9 \text{ \AA}$ and for large δ the dominant term is δ^{-3} . Here, given the empirical nature of this fit, we focus on the more widely applicable δ^{-4} form for bilayer materials.

There are four δ -independent functions in Eq. (3), i.e., A , B , α , and d . d as a function of ϕ and ψ were reported above. Focusing on the behavior of Γ in the vicinity of the relaxed interlayer spacing $d(\phi, \psi)$, we can determine A , B , and α from the three conditions:

$$\begin{aligned} \Gamma(\phi, \psi, \delta) \Big|_{\delta=d(\phi, \psi)} &= \gamma(\phi, \psi), \\ \frac{\partial \Gamma(\phi, \psi, \delta)}{\partial \delta} \Big|_{\delta=d(\phi, \psi)} &= 0, \\ \frac{\partial^2 \Gamma(\phi, \psi, \delta)}{\partial \delta^2} \Big|_{\delta=d(\phi, \psi)} &= \frac{C_{nn}(\phi, \psi)}{d(\phi, \psi)} \equiv \kappa(\phi, \psi), \end{aligned} \quad (4)$$

where $C_{nn}(\phi, \psi)$ is the $\mathbf{n} \otimes \mathbf{n}$ component of the elastic constant tensor at each (ϕ, ψ) disregistry state. In principle, A , B , and α in Eq. (3) can be determined by Eq. (4) if the functions $\gamma(\phi, \psi)$, $d(\phi, \psi)$, and $C_{nn}(\phi, \psi)$ are known. $\gamma(\phi, \psi)$ and $d(\phi, \psi)$ have been obtained by fitting Eq. (2) to the ACFDT-RPA results in Section IV. However, the accurate ACFDT-RPA calculation of $C_{nn}(\phi, \psi)$ was considered to computationally costly for direct calculation. Our strategy to limit such computation is to ignore the ϕ - and ψ -dependence of $\partial^2 \Gamma / \partial \delta^2$ and instead use $\kappa = \kappa_0 \equiv C_{nn,0}/d_0$ evaluated at the equilibrium registry ($\phi = 0, \psi = 0$). In this way, Eq. (4) becomes

$$\begin{aligned} \alpha &= \left\{ -[\kappa_0 d^2 - 20(\gamma - \gamma_{\text{coh}})] \right. \\ &\quad \left. + \sqrt{[\kappa_0 d^2 - 20(\gamma - \gamma_{\text{coh}})]^2 + 64\kappa_0 d^2 (\gamma - \gamma_{\text{coh}})} \right\} \\ &\quad / [8d(\gamma - \gamma_{\text{coh}})], \\ A &= [4(\gamma - \gamma_{\text{coh}}) \exp(\alpha d)] / (4 - \alpha d), \\ B &= [\alpha d(\gamma - \gamma_{\text{coh}})] / (4 - \alpha d). \end{aligned} \quad (5)$$

Based on Eq. (3) and Eq. (5), extension of the GSFE to three dimensions requires only one additional material parameter $\kappa_0 = C_{nn}(\phi = 0, \psi = 0)/d_0 = C_{nn,0}/d_0$.

In order to validate the simple form of Eq. (3) and to ensure that the assumption $\kappa(\phi, \psi) = \kappa_0$ is reasonable, we compare the G/G bilayer data directly calculated by DFT-D2 for a set of (ϕ, ψ, δ) and the Γ hypersurface constructed according to Eq. (3) with the fitted $\gamma(\phi, \psi)$ and $d(\phi, \psi)$. First, we examine the behavior of $\Gamma(\phi', \psi', \delta)$, where (ϕ', ψ') correspond to the AB, AA, and SP states (see Fig. 8). Overall, the Γ versus δ curves show the correct behavior, especially near the minimum for all three registries. The agreement is especially good near the min-

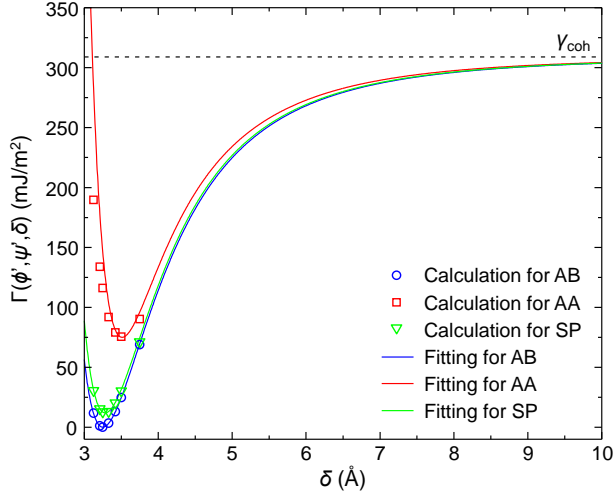


FIG. 8. The plot of $\Gamma(\phi', \psi', \delta)$ based on the DFT-D2 calculations of G/G. The curves are constructed according to Eq. (3) with the fitted $\gamma(\phi, \psi)$ and $d(\phi, \psi)$; the points denote the raw data directly obtained by DFT-D2 calculations. (ϕ', ψ') is taken to be associated with AB ($\phi' = 0, \psi' = 0$), AA ($\phi' = 0, \psi' = a_0/\sqrt{3}$), and SP ($\phi' = 0, \psi' = 5\sqrt{3}a_0/6$) disregistry states.

ima $\delta = d(\phi', \psi')$, where the fit was performed. Slight deviations between the calculations and the fit are observed only for the AA state (corresponding to a maximum in $\gamma(\phi, \psi)$); however, this is of little significance since this corresponds to the most unstable disregistry (i.e., one which would likely never be observed in equilibrium or in dynamic processes). Next, we examine $\Gamma(\phi, \psi, \delta')$ for several interlayer spacings near the minimum in δ ; see the comparison of these fit forms with those obtained directly from the DFT-D2 calculations in Fig. 9. The upper panels of this figure show the DFT-D2 calculations (first row) and fit landscapes (second row) and the lower panel of Fig. 9 shows the same comparison along $[1\bar{1}00]$. These results shows that the fitted Γ profile (Eq. (3)) agrees well with the direct calculation data except near the peak in $\gamma(\phi, \psi)$; the minimum at AB and the saddle point at SP are accurately determined. The deviation near the peak can be understood from the constraints employed in fitting. The first constraint in Eq. (4) on the $\Gamma(\phi, \psi; \delta)$ is that, for each state (ϕ, ψ) , when the interlayer spacing δ is at its equilibrium value $d(\phi, \psi)$, i.e., $\Gamma(\phi, \psi; \delta)$ is exactly equal to $\gamma(\phi, \psi)$. Naturally, the deviation between the fitted form of $\Gamma(\phi, \psi; \delta)$ and the DFT-D2 results arises with increasing deviation of the interlayer spacing from where the fitting was done, i.e., $d(\phi, \psi)$. Indeed, we find that the fit is excellent for the AA state near $\delta = 1.02d_0$ (close to equilibrium spacing for AA; Fig. 9(i)) and gets worse as the spacing decreases from d_0 (Fig. 9(h)) to $0.962d_0$ (Fig. 9(g)). Also, the third constraint in Eq. (4) and the assumption that $\kappa(\phi, \psi) = \kappa_0$ guarantee that the deviation of the fitted Γ profile from the DFT results is always small near the stable state (AB state). As the result of mechanical deformation, the local structure will

be dominated by the stable state (which we reproduce by design) and the path between stable and/or metastable states; fig. 9 shows that we properly reproduce the energy associated with all states between these (including the saddle-point state).

Given the function Eq. (3) works so well as δ varies around $d(\phi, \psi)$ based on the DFT-D2 data, we employed the same strategy with input data obtained from the ACFDT-RPA calculations to make accurate three-dimensional GSFE predictions. The $\Gamma(\phi, \psi, \delta')$ surfaces fit to the ACFDT-RPA data are shown in Fig. 10, where $\delta'/d_0 = 0.95, 1, 1.05$, and 1.15 , each for G/G, BN/BN-1, and G/BN bilayer systems. The Γ hypersurfaces obtained here are accurate in the sense that they are parameterized via the accurate ACFDT-RPA data; they are expected to be valid at least near the minimum interlayer spacings and be reasonable at all interlayer spacings accessible to experiments (e.g., elastic deformation, bilayer formation and decohesion, interlayer sliding⁵⁹, and bilayer-dislocation-core distortion⁵⁸).

In summary, the three-dimensional generalized stacking-fault energy is

$$\Gamma(\gamma, d; \delta) = A(\gamma, d)e^{-\alpha(\gamma, d)\delta} - B(\gamma, d)\left(\frac{d}{\delta}\right)^4 + \gamma_{\text{coh}}, \quad (6)$$

where, of course, γ and d are functions of ϕ and ψ . In this way, the complete three-dimensional GSFE can be written using this function where $A(\gamma, d)$, $B(\gamma, d)$, and $\alpha(\gamma, d)$ are given in Eq. (5), and $\gamma(\phi, \psi)$ and $d(\phi, \psi)$ are given explicitly in Eq. (2) with parameters from Table III. The remaining parameters in Eq. (5) are γ_{coh} and $\kappa_0 \equiv C_{nn,0}/d_0$ which may be obtained directly from Table II.

VI. BAND-GAP LANDSCAPES

Finally, just in order to exemplify how the disregistry states determines the local properties of bilayers, we present the calculation of band gap as a function of disregistry.

The electronic band structure of a bilayer system can be modified by changing the disregistry of one layer with respect to the other. The presence of defects such as interlayer dislocations and twist boundaries can locally produce such variation in disregistry and thus induce spatial variation in the band structure on a length scale that can be manipulated by, for example, changing twist angle between layers or by choosing van der Waals layers which are misfitting with respect to one another (heterobilayers). It has been proposed that spatial variations in the band gap can be used to funnel excitons into local band gap minimum regions; this mechanism can be used for solar energy harvesting and electroluminescence⁶⁰. Local variations in band gap should be observable using scanning tunneling spectroscopy (STS); macroscopic changes in band structure with layer rotation in bilayer graphene has been observed via Raman spectroscopy

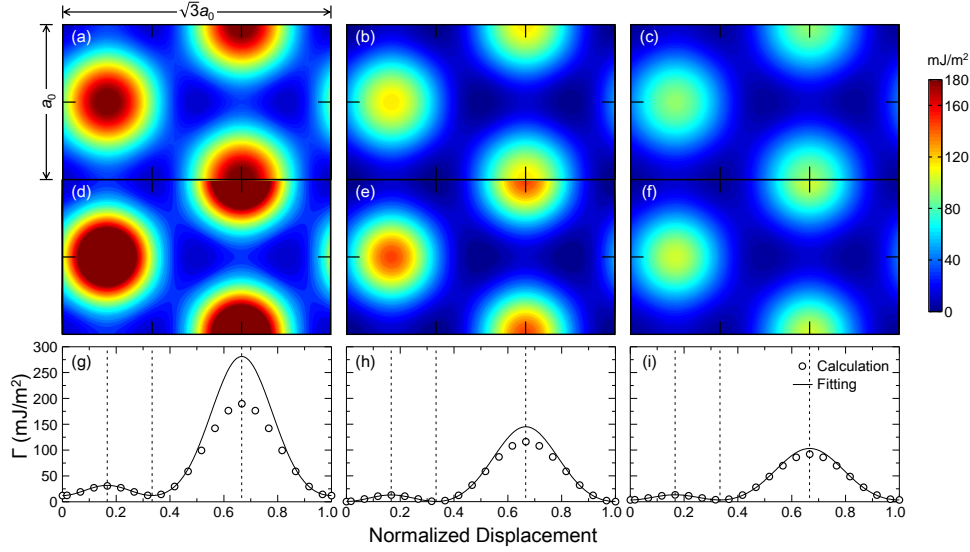


FIG. 9. The G/G $\Gamma(\phi, \psi, \delta')$ surfaces obtained directly from the DFT-D2 data at (a) $\delta'/d_0 = 0.962$, (b) $\delta'/d_0 = 1$, and (c) $\delta'/d_0 = 1.02$, and those derived from Eq. (3) parameterized by the data at (d) $\delta'/d_0 = 0.962$, (e) $\delta'/d_0 = 1$, and (f) $\delta'/d_0 = 1.02$. The corresponding Γ profiles along $[1\bar{1}00]$ are shown in (g), (h), and (i).

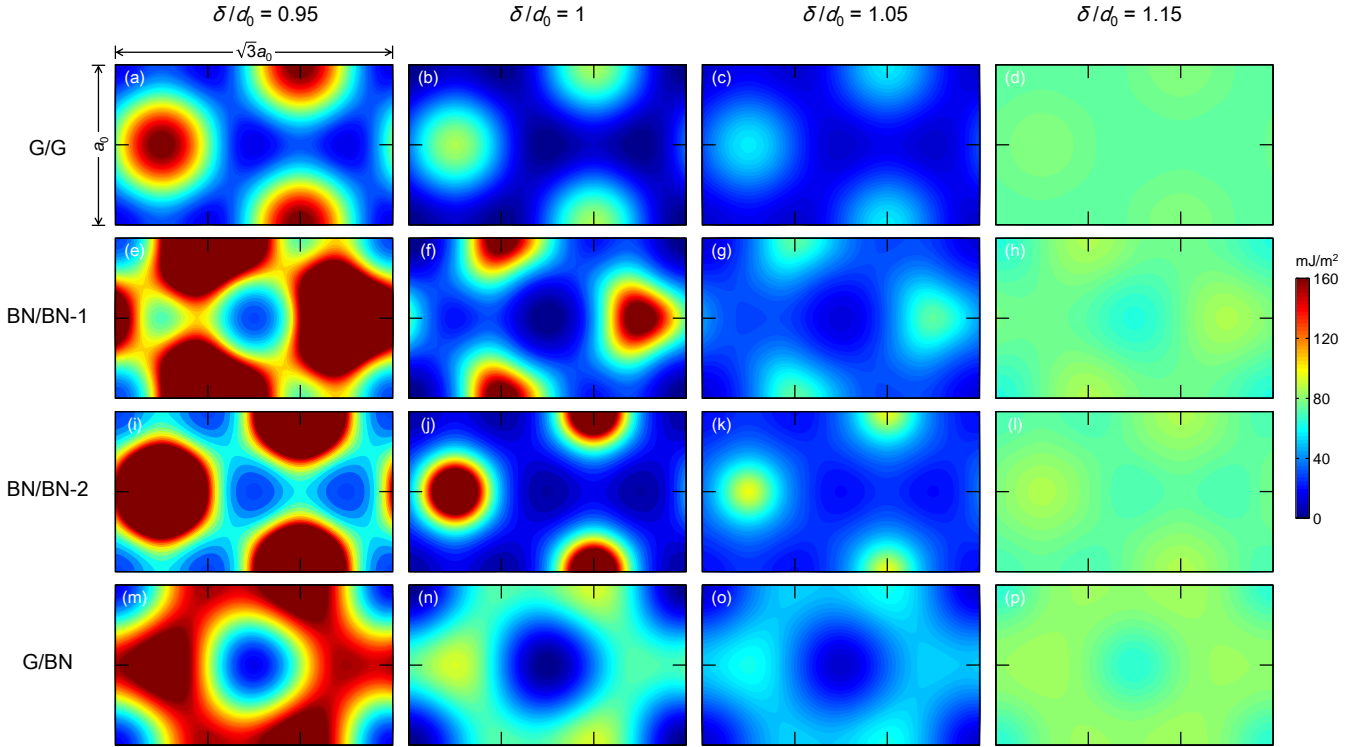


FIG. 10. The $\Gamma(\phi, \psi, \delta')$ surfaces for G/G (a-d), BN/BN-1 (e-h), BN/BN-2 (i-l) and G/BN (m-p) derived from Eq. (3) and parameterized by the ACFDT-RPA data at $\delta'/d_0 = 0.95, 1, 1.05$, and 1.1 .

(and explained theoretically)^{61,62}. The implementation of such band gap engineering relies on knowledge of the spatial variation of disregistry ($\phi(\mathbf{r}), \psi(\mathbf{r})$) and the band gap versus disregistry landscape $E_g(\phi, \psi)$. The disregistry distribution ($\phi(\mathbf{r}), \psi(\mathbf{r})$) associated with interlayer twist or misfit dislocations can be obtained by minimizing

the total energy including the interlayer bonding energy $\gamma(\phi, \psi)$ and elastic strain energy (e.g., using the Peierls-Nabarro model¹⁶). Here, we report the band gap landscapes $E_g(\phi, \psi)$ for G/G, BN/BN, and G/BN bilayer systems.

The two steps in the calculation of $E_g(\phi, \psi)$ for each

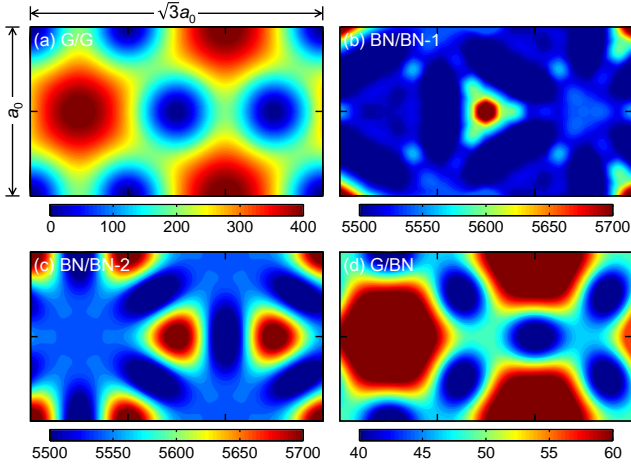


FIG. 11. The band-gap (meV) landscapes for (a) G/G, (b) BN/BN-1, (c) BN/BN-2, and (d) G/BN. Note that the LDA results in (b) and (c) were shifted by 1470 meV and the LDA results in (d) by 5 meV to be consistent with HSE calculations.

bilayer system are (1) determining the relaxed interlayer spacing versus disregistry $d(\phi, \psi)$ and (2) determining the band gap as a function of disregistry at the appropriate interlayer spacing.

The first step was reported above using the ACFDT-RPA method. It is noted that the reasonable band gap can be obtained on the premise that the disregistry structure (particularly relaxed interlayer spacing) is correct. The fitting scheme proposed above enables us to obtain the reliable disregistry structure based on ACFDT-RPA approach; without such strategy, it is impossible to obtain the reliable band gap even if the band-gap calculation method is absolutely accurate.

For the second step, we determine the band gap by combining the results of conventional LDA functional and HSE hybrid functional⁶³. Since calculations using the LDA are computationally efficient, we map out the entire band-gap landscapes via an LDA functional. However, it is well-known that the band gaps of semiconductors and insulators are commonly underestimated using LDA⁶⁴ (such systematic error is attributed to the fact that in the LDA the energy versus number of charges is convex rather than linear⁶⁵). It has been shown that hybrid functionals, such as HSE, can effectively avoid this problem⁶⁵ and, indeed, HSE yields reliable band-gap for many semiconductors⁶⁶. However, it is impractical to produce the entire band-gap landscapes using HSE since such calculation are computationally costly. Our strategy is to shift the LDA results by a constant value determined from the data for a few disregistry states produced by HSE (see Supplemental Material for details).

Figure 11 shows the band-gap landscapes for G/G, BN/BN-1, BN/BN-2, and G/BN. For G/G (Fig. 11a), the band gap vanishes at the equilibrium AB registry state; this is consistent with the well-known result that the ground-state bilayer graphene is metallic⁶⁷. Al-

though the band gap can be opened up to 400 meV as the unstable AA state is reached, this state can never be accessed in any local position of a G/G bilayer or during a realistic mechanical process. The maximum band gap that might be actually achieved is about 200 meV, corresponding to the SP state, since the SP state may locally exist in the core of a bilayer dislocation. For G/BN (Fig. 11d), the variation of band gap with the change of disregistry is very small (only 30 meV). It shows that $E_g(\text{unstable AA state}) > E_g(\text{unstable AB' state}) > E_g(\text{stable AB state})$; such order is consistent with the results of earlier study⁷ (although in the earlier study the relaxed interlayer spacing was obtained by LDA rather than ACFDT-RPA). In general, BN/BN has much larger band gap than G/G and G/BN. For BN/BN-1 (Fig. 11b), the maximum band gap is about 5.8 eV, which occurs at the stable AA' registry state. Beyond the AA' state, the variation of band gap is mild with the change of disregistry (including the metastable AB' state). The minimum band gap occurs near the saddle point (about 5.5 eV). The situation of BN/BN-2 is quite similar to that of BN/BN-1, i.e., the maximum and minimum band gaps correspond to the stable state and the saddle point, respectively, and they are also at the same scale as the band gaps of the respective states in BN/BN-1.

Figure 11 shows the band-gap landscapes for G/G, BN/BN-1, BN/BN-2, and G/BN. For G/G (Fig. 11a), the band gap vanishes at the equilibrium AB registry state; this is consistent with the well-known result that the ground-state of bilayer graphene is metallic⁶⁷. Although the band gap can be as wide as 400 meV at the most unstable disregistry (the AA state), this state will likely never be accessed anywhere in the G/G bilayer (including at dislocation cores) or during realistic mechanical processes (e.g., sliding). We suspect that the maximum band gap that will be observable in spots in a G/G bilayer may be ~ 200 meV, corresponding to the SP state, since the saddle-point configuration may exist within the core of a bilayer dislocation. For G/BN (Fig. 11d), the variation of band gap with the change of disregistry is very small (only 30 meV). It shows that $E_g(\text{unstable AA state}) > E_g(\text{unstable AB' state}) > E_g(\text{stable AB state})$; this order is consistent with the results of an earlier study⁷ (although in the earlier study the relaxed interlayer spacing was obtained by LDA rather than ACFDT-RPA). In general, BN/BN has a much larger band gap than G/G and G/BN. For BN/BN-1 (Fig. 11b), the maximum band gap is ~ 5.8 eV, which occurs at the stable AA' registry state. Beyond the AA' state, the variation of the band gap with disregistry is small (including the metastable AB' state). The minimum band gap occurs near the saddle point (~ 5.5 eV). The situation for BN/BN-2 is quite similar to that of BN/BN-1, i.e., the maximum and minimum band gaps (and their magnitude) correspond to the stable state and the saddle point in both BN/BN-1 and BN/BN-2, respectively.

VII. DISCUSSION AND CONCLUSIONS

The structure, energy, and band structure of G/G, BN/BN, and G/BN bilayers are functions of the registry between the layers. An accurate determination of the bilayer structure and energy depends sensitively on the manner in which the dispersion interactions are treated. We found that, while many of the corrections methods employed today for the determination of these interactions can lead to qualitatively correct trends in the bilayer energy and the relaxed interlayer spacing with disregistry, only the ACFDT-RPA method (amongst all of the methods tested) leads to reliable quantitative predictions. Unfortunately, the computational cost for the ACFDT-RPA method is high. This makes its routine application in situations where a large number of calculations are required prohibitive. Such a case is the determination of the energy as a function of disregistry and interlayer spacing – our focus in this report.

In order to overcome the difficulty associated with this high computational cost, we adopted the following strategy. First, we calculated the relaxed interlayer spacing and energy as a function of disregistry using the computationally efficient DFT-D2 method and demonstrated that these results could be accurately fitted to an empirical function that respects the bilayer symmetry. We also demonstrated that this fit can be obtained with excellent accuracy based on a small number of disregistries. Using this validated fitting approach, we then obtained the requisite data for fitting the bilayer energy and interlayer spacing functions using the accurate ACFDT-RPA method. This approach allowed us to accurately determine the entire energy and relaxed interlayer spacing landscapes at reasonable computational cost. These landscapes provide an accurate prediction of not only the equilibrium bilayer structural state, but also the metastable states and the barriers between these states. Such barriers are upper bounds on the resistance to layer sliding.

The bilayer energy as a function of disregistry (the generalized stacking-fault energy) is important for the determination of defect structures in bilayers. For example, edge dislocations are intrinsic features in many hetero-bilayer systems, such as G/BN, where they can account for the mismatch in lattice constants. The ex-

tended dislocation core structure of such hetero-bilayer structures is sensitive to the generalized stacking-fault energy. With only the generalized stacking-fault energy and the elastic constants of the individual layers as input, a generalized Peierls-Nabarro model^{57,68,69} can be formulated to predict detailed dislocation structure.

Equally interesting is the case where the two layers in a homo- or hetero-bilayer structure are rotated with respect to one another. Such twisted bilayers have been described as a Moiré structures, although the actual structure will be considerably different and more appropriately described as composed of a two-dimensional periodic array of screw dislocations, at least at small twist angles. This structure too can be predicted using the same type of generalized Peierls-Nabarro model^{16,57,68,69}.

Using the relaxed interlayer spacing and energy results, we also calculated the band-gap landscapes by correction scheme: correct the band gap produced by LDA functional according to the fewer data obtained by HSE functional. These results show that the band gap varies in the range of 0–0.4 eV in G/G, 5.5–5.8 eV (5%) in BN/BN, and 0.04–0.07 eV (100%) in G/BN. This implies that in both homo-bilayer systems, where the two layers are rotated relative to each other, and hetero-bilayer systems with or without rotation, the band gap will vary from region to region through the bilayer. Such a variation should be directly observable using scanning tunneling spectroscopy. For the case of homo-bilayer rotation, this will lead to a two-dimensional periodic band structure with the periodicity determined by the twist angle⁷⁰. These periodic variations in band structure can lead to an electronic metamaterial behavior that can be used to engineer excitonic behavior to tailor properties. The present band gap and generalized stacking-fault energy provide the basis for future prediction of defect structure and electronic behavior of homo- and hetero-structured van der Waals layered systems.

VIII. ACKNOWLEDGEMENTS

The authors gratefully acknowledge fruitful discussions with Prof. Steven Louie (University of California, Berkeley) and Prof. Eugene Mele (University of Pennsylvania). This work was supported the Office of Sciences, Basic Energy Sciences, Department of Energy through the EFRC award, DE-SC0012575.

¹ A. K. Geim and K. S. Novoselov, *Nat. Mater.* **6**, 183 (2007).

² M. I. Katsnelson, K. S. Novoselov, and A. K. Geim, *Nat. Phys.* **2**, 620 (2006).

³ K. S. Novoselov, A. K. Geim, S. V. Morozov, D. Jiang, M. I. Katsnelson, I. V. Grigorieva, S. V. Dubonos, and A. A. Firsov, *Nature* **438**, 197 (2005).

⁴ Y. Zhang, Y.-W. Tan, H. L. Stormer, and P. Kim, *Nature* **438**, 201 (2005).

⁵ K. S. Novoselov, E. McCann, S. V. Morozov, V. I. Fal'ko, M. I. Katsnelson, U. Zeitler, D. Jiang, F. Schedin, and A. K. Geim, *Nat. Phys.* **2**, 177 (2006).

⁶ E. McCann and V. I. Fal'ko, *Phys. Rev. Lett.* **96**, 086805 (2006).

⁷ G. Giovannetti, P. A. Khomyakov, G. Brocks, P. J. Kelly, and J. van den Brink, *Phys. Rev. B* **76**, 073103 (2007).

- ⁸ C. R. Dean, A. F. Young, I. Meric, C. Lee, L. Wang, S. Sorgenfrei, K. Watanabe, T. Taniguchi, P. Kim, K. L. Shepard, and J. Hone, *Nat. Nanotechnol.* **5**, 722 (2010).
- ⁹ L. Britnell, R. V. Gorbachev, R. Jalil, B. D. Belle, F. Schedin, A. Mishchenko, T. Georgiou, M. I. Katsnelson, L. Eaves, S. V. Morozov, N. M. R. Peres, J. Leist, A. K. Geim, K. S. Novoselov, and L. A. Ponomarenko, *Science* **335**, 947 (2012).
- ¹⁰ G. Li, A. Luican, J. L. Dos Santos, A. C. Neto, A. Reina, J. Kong, and E. Andrei, *Nature Physics* **6**, 109 (2009).
- ¹¹ J. M. B. Lopes dos Santos, N. M. R. Peres, and A. H. Castro Neto, *Phys. Rev. Lett.* **99**, 256802 (2007).
- ¹² Z. Y. Rong and P. Kuiper, *Phys. Rev. B* **48**, 17427 (1993).
- ¹³ W.-T. Pong and C. Durkan, *J. Phys. D* **38**, R329 (2005).
- ¹⁴ V. Vitek, *Philos. Mag.* **18**, 773 (1968).
- ¹⁵ S. Dai, Y. Xiang, and D. J. Srolovitz, *Acta Mater.* **61**, 1327 (2013).
- ¹⁶ S. Dai, Y. Xiang, and D. J. Srolovitz, *Acta Mater.* **69**, 162 (2014).
- ¹⁷ X. Gong and E. J. Mele, *Phys. Rev. B* **89**, 121415 (2014).
- ¹⁸ C. Lee, Q. Li, W. Kalb, X.-Z. Liu, H. Berger, R. W. Carpick, and J. Hone, *Science* **328**, 76 (2010).
- ¹⁹ N. Marom, J. Bernstein, J. Garel, A. Tkatchenko, E. Joselevich, L. Kronik, and O. Hod, *Phys. Rev. Lett.* **105**, 046801 (2010).
- ²⁰ G. Constantinescu, A. Kuc, and T. Heine, *Phys. Rev. Lett.* **111**, 036104 (2013).
- ²¹ J. Jung, A. Raoux, Z. Qiao, and A. H. MacDonald, *Phys. Rev. B* **89**, 205414 (2014).
- ²² W. Gao and A. Tkatchenko, *Phys. Rev. Lett.* **114**, 096101 (2015).
- ²³ C. Brandl, P. M. Derlet, and H. Van Swygenhoven, *Phys. Rev. B* **76**, 054124 (2007).
- ²⁴ P. S. Branicio, J. Y. Zhang, and D. J. Srolovitz, *Phys. Rev. B* **88**, 064104 (2013).
- ²⁵ P. Hobza, J. Šponer, and T. Reschel, *J. Comput. Chem.* **16**, 1315 (1995).
- ²⁶ S. Kristyán and P. Pulay, *Chem. Phys. Lett.* **229**, 175 (1994).
- ²⁷ A. Stone, *The theory of intermolecular forces* (Oxford University Press, 2013).
- ²⁸ S. Grimme, *J. Comput. Chem.* **27**, 1787 (2006).
- ²⁹ K. Lee, É. D. Murray, L. Kong, B. I. Lundqvist, and D. C. Langreth, *Phys. Rev. B* **82**, 081101 (2010).
- ³⁰ J. Klimeš, D. R. Bowler, and A. Michaelides, *Phys. Rev. B* **83**, 195131 (2011).
- ³¹ J. Sun, B. Xiao, and A. Ruzsinszky, *J. Chem. Phys.* **137**, 051101 (2012).
- ³² J. Sun, R. Haunschild, B. Xiao, I. W. Bulik, G. E. Scuseria, and J. P. Perdew, *J. Chem. Phys.* **138**, 044113 (2013).
- ³³ J. Sun, B. Xiao, Y. Fang, R. Haunschild, P. Hao, A. Ruzsinszky, G. I. Csonka, G. E. Scuseria, and J. P. Perdew, *Phys. Rev. Lett.* **111**, 106401 (2013).
- ³⁴ J. Harl and G. Kresse, *Phys. Rev. B* **77**, 045136 (2008).
- ³⁵ J. Harl and G. Kresse, *Phys. Rev. Lett.* **103**, 056401 (2009).
- ³⁶ J. Harl, L. Schimka, and G. Kresse, *Phys. Rev. B* **81**, 115126 (2010).
- ³⁷ P. Hyldgaard, K. Berland, and E. Schröder, *Phys. Rev. B* **90**, 075148 (2014).
- ³⁸ Y. Andersson, E. Hult, H. Rydberg, P. Apell, B. I. Lundqvist, and D. C. Langreth, in *Electronic Density Functional Theory* (Springer, 1998) pp. 243–260.
- ³⁹ G. K. H. Madsen, L. Ferrighi, and B. Hammer, *J. Phys. Chem. Lett.* **1**, 515 (2009).
- ⁴⁰ M. Andersen, L. Hornekær, and B. Hammer, *Phys. Rev. B* **86**, 085405 (2012).
- ⁴¹ S. Lebegue, J. Harl, T. Gould, J. G. Ángyán, G. Kresse, and J. F. Dobson, *Phys. Rev. Lett.* **105**, 196401 (2010).
- ⁴² J. P. Perdew, K. Burke, and M. Ernzerhof, *Phys. Rev. Lett.* **77**, 3865 (1996).
- ⁴³ G. Kresse and J. Hafner, *Phys. Rev. B* **47**, 558 (1993).
- ⁴⁴ G. Kresse and J. Hafner, *Phys. Rev. B* **49**, 14251 (1994).
- ⁴⁵ G. Kresse and J. Furthmüller, *Comput. Mater. Sci.* **6**, 15 (1996).
- ⁴⁶ G. Kresse and J. Furthmüller, *Phys. Rev. B* **54**, 11169 (1996).
- ⁴⁷ P. E. Blöchl, *Phys. Rev. B* **50**, 17953 (1994).
- ⁴⁸ G. Kresse and D. Joubert, *Phys. Rev. B* **59**, 1758 (1999).
- ⁴⁹ Y. Baskin and L. Meyer, *Phys. Rev.* **100**, 544 (1955).
- ⁵⁰ O. L. Blakslee, D. G. Proctor, E. J. Seldin, G. B. Spence, and T. Weng, *J. Appl. Phys.* **41**, 3373 (1970).
- ⁵¹ R. S. Pease, *Nature* **165**, 722 (1950).
- ⁵² J. F. Green, T. K. Bolland, and J. W. Bolland, *J. Chem. Phys.* **64**, 656 (1976).
- ⁵³ S. J. Haigh, A. Gholinia, R. Jalil, S. Romani, L. Britnell, D. C. Elias, K. S. Novoselov, L. A. Ponomarenko, A. K. Geim, and R. Gorbachev, *Nat. Mater.* **11**, 764 (2012).
- ⁵⁴ C. H. Lui, Z. Li, Z. Chen, P. V. Klimov, L. E. Brus, and T. F. Heinz, *Nano Lett.* **11**, 164 (2010).
- ⁵⁵ A. Marini, P. García-González, and A. Rubio, *Phys. Rev. Lett.* **96**, 136404 (2006).
- ⁵⁶ While the MGGA-MS2 is a semi-local functional that captures the intermediate-range van der Waals interaction^{31–33}, it does not capture the long-range van der Waals interaction (it is only effective where there is significant electron density overlap). Clearly, the long-range van der Waals interaction exists in the layered materials even without such electron density overlap. Since the MGGA-MS2 does not include this term, it underestimates the cohesive energy in these systems.
- ⁵⁷ Y. Xiang, H. Wei, P. Ming, and W. E, *Acta Mater.* **56**, 1447 (2008).
- ⁵⁸ B. Butz, C. Dolle, F. Niekel, K. Weber, D. Waldmann, H. B. Weber, B. Meyer, and E. Spiecker, *Nature* (2013).
- ⁵⁹ X. Feng, S. Kwon, J. Y. Park, and M. Salmeron, *ACS Nano* **7**, 1718 (2013).
- ⁶⁰ M. Wu, X. Qian, and J. Li, *Nano Lett.* **14**, 5350 (2014).
- ⁶¹ K. Kim, S. Coh, L. Z. Tan, W. Regan, J. M. Yuk, E. Chatterjee, M. F. Crommie, M. L. Cohen, S. G. Louie, and A. Zettl, *Phys. Rev. Lett.* **108**, 246103 (2012).
- ⁶² S. Coh, L. Z. Tan, S. G. Louie, and M. L. Cohen, *Phys. Rev. B* **88**, 165431 (2013).
- ⁶³ J. Heyd, G. E. Scuseria, and M. Ernzerhof, *J. Chem. Phys.* **118**, 8207 (2003).
- ⁶⁴ G. Onida, L. Reining, and A. Rubio, *Rev. Mod. Phys.* **74**, 601 (2002).
- ⁶⁵ P. Mori-Sánchez, A. J. Cohen, and W. Yang, *Phys. Rev. Lett.* **100**, 146401 (2008).
- ⁶⁶ J. Heyd, J. E. Peralta, G. E. Scuseria, and R. L. Martin, *J. Chem. Phys.* **123**, 174101 (2005).
- ⁶⁷ Y. Zhang, T.-T. Tang, C. Girit, Z. Hao, M. C. Martin, A. Zettl, M. F. Crommie, Y. R. Shen, and F. Wang, *Nature* **459**, 820 (2009).
- ⁶⁸ R. Peierls, *Proc. Phys. Soc. (London)* **52**, 34 (1940).

- ⁶⁹ F. R. N. Nabarro, Proc. Phys. Soc. (London) **59**, 256 (1947).
- ⁷⁰ R. Bistritzer and A. H. MacDonald, Proc. Natl. Acad. Sci. USA **108**, 12233 (2011).